

# On the Role of Physical Processes in Controlling Equatorial Plasma Bubble Morphology

Giorgio Arlan da Silva Picanço<sup>1</sup>, Clezio Marcos Denardini<sup>2</sup>, Paulo Alexandre Bronzato Nogueira<sup>3</sup>, Paulo Roberto Fagundes<sup>4</sup>, Amalia Meza<sup>5</sup>, Luciano Pedro Oscar Mendoza<sup>6</sup>, Marcelo Banik Pádua<sup>2</sup>, María Paula Natali<sup>7</sup>, Laysa Cristina Araujo Resende<sup>8</sup>, and Luiz Phillip Rodrigues Vital<sup>9</sup>

<sup>1</sup>University of Vale of Paraíba (UNIVAP)

<sup>2</sup>National Institute for Space Research

<sup>3</sup>Federal Institute of Education, Science and Technology of Sao Paulo

<sup>4</sup>Universidade do Vale do Paraíba - UNIVAP

<sup>5</sup>MAGGIA Laboratory, Facultad de Cs. Astronomicas y Geofisicas de La Plata and CONICET

<sup>6</sup>Universidad Nacional de La Plata

<sup>7</sup>Laboratorio de Meteorología espacial, Atmósfera terrestre, Geodesia, Geodinámica, diseño de Instrumental y Astrometría (MAGGIA), Facultad de Ciencias Astronómicas y Geofísicas (FCAG), Universidad Nacional de La Plata (UNLP), CONICET

<sup>8</sup>National Institute for Space Research/China-Brazil Joint Laboratory of Space Weather

<sup>9</sup>Instituto Nacional de Pesquisas Espaciais

April 24, 2024

## Abstract

In this study, we present the results of an analysis of the morphological features of Equatorial Plasma Bubbles (EPBs) over South America. In this context, we analyzed data from the Disturbance Ionosphere index (DIX) maps calculated using around 450 Global Navigation Satellite System (GNSS) stations. To mitigate the influence of magnetic disturbances on bubble development, only data from geomagnetically quiet days were utilized. This study covered the period from the post-peak of solar cycle 24 (2015) to the pre-peak of solar cycle 25 (2023), totaling 1321 nights with EPB occurrences, representing the largest dataset of EPBs ever compiled for South America. Our analysis unveiled several key findings regarding EPBs and their behavior over the South American region. Firstly, we observed that the amplitude of plasma depletions and the EPB latitudinal development follow an approximately 11-year cycle driven by solar radiation levels. Furthermore, our analysis highlights the significant influence of factors such as vertical plasma drift velocity during the pre-reversal enhancement (PRE), longitudinal variations associated with magnetic declination, as well as the saturation behavior of EPB development with extreme solar flux. Finally, we outline an empirical model to calculate the maximum latitudinal extent of EPBs based on solar flux and magnetic declination as an attempt to provide insights for anticipating EPB behavior across different solar cycle stages and in different longitude sectors.

## Hosted file

Picanco et al. (2024) - JGR Manuscript.docx available at <https://authorea.com/users/162992/articles/857041-on-the-role-of-physical-processes-in-controlling-equatorial-plasma-bubble-morphology>

# On the Role of Physical Processes in Controlling Equatorial Plasma Bubble Morphology

G.A.S. Picanço<sup>1</sup>, C.M. Denardini<sup>2</sup>, P.A.B. Nogueira<sup>3</sup>, P.R. Fagundes<sup>1</sup>, A.M. Meza<sup>4</sup>, L.P.O. Mendoza<sup>4</sup>, M.B. Pádua<sup>2</sup>, M.P. Natali<sup>4</sup>, L.C.A. Resende<sup>2,5</sup>, and L.F.R. Vital<sup>2</sup>

<sup>1</sup> Research and Development Institute, University of Vale of Paraíba (IP&D/UNIVAP), São José dos Campos, Brazil.

<sup>2</sup> National Institute for Space Research (INPE), São José dos Campos, Brazil.

<sup>3</sup> Federal Institute of Education, Science and Technology of São Paulo (IFSP), Jacareí, Brazil.

<sup>4</sup> Faculty of Astronomical and Geophysical Sciences, National University of La Plata (FCAG/UNLP), La Plata, Argentina.

<sup>5</sup> National Space Science Center, Chinese Academy of Sciences (NSSC/CAS), Beijing, China.

Corresponding author: Giorgio Picanço (giorgio.picanco@gmail.com)

Physics and Astronomy Laboratory, Research and Development Institute, University of Vale of Paraíba (IP&D/UNIVAP), Av. Shishima Hifumi, 2911, Urbanova, 12244-010, São José dos Campos, SP, Brazil; Phone: +55 12 3947-1146.

## Key Points:

- EPB behavior exhibits a cycle linked with solar flux levels, impacting plasma depletion amplitudes and latitudinal development according to magnetic declination sector.
- During geomagnetically quiet periods, the development of EPBs reveals a saturation point for extreme solar flux values, beyond which the intensification of EPBs ceases to be significant.
- An empirical model is outlined to calculate the maximum latitudinal extent of EPBs based on solar flux and magnetic declination, aiming to provide insights for anticipating EPB behavior across different solar cycle stages and in different longitudinal sectors.

## Abstract

In this study, we present the results of an analysis of the morphological features of Equatorial Plasma Bubbles (EPBs) over South America. In this context, we analyzed data from the Disturbance Ionosphere index (DIX) maps calculated using around 450 Global Navigation Satellite System (GNSS) stations. To mitigate the influence of magnetic disturbances on bubble development, only data from geomagnetically quiet days were utilized. This study covered the period from the post-peak of solar cycle 24 (2015) to the pre-peak of solar cycle 25 (2023), totaling 1321 nights with EPB occurrences, representing the largest dataset of EPBs ever compiled for South America. Our analysis unveiled several key findings regarding EPBs and

38 their behavior over the South American region. Firstly, we observed that the amplitude of plasma  
39 depletions and the EPB latitudinal development follow an approximately 11-year cycle driven by  
40 solar radiation levels. Furthermore, our analysis highlights the significant influence of factors  
41 such as vertical plasma drift velocity during the pre-reversal enhancement (PRE), longitudinal  
42 variations associated with magnetic declination, as well as the saturation behavior of EPB  
43 development with extreme solar flux. Finally, we outline an empirical model to calculate the  
44 maximum latitudinal extent of EPBs based on solar flux and magnetic declination as an attempt  
45 to provide insights for anticipating EPB behavior across different solar cycle stages and in  
46 different longitude sectors.

47

## 48 **1 Introduction**

49 Equatorial Plasma Bubbles (EPBs) are ionospheric phenomena characterized by F-region  
50 irregularities, where plasma density is significantly reduced when compared with adjacent  
51 regions (Kelley, 2009). The process of EPB generation primarily arises from plasma instabilities  
52 propagating from lower-density regions (below the F2 layer) to altitudes where the density is  
53 higher (the F2 layer) (Haerendel, 1973). The nonlinear evolution of Rayleigh-Taylor Instability  
54 (RTI) is the widely accepted primary mechanism for EPB generation in the ionosphere, arising  
55 from the upward propagation of this low-density plasma. The RTI initiates through the  
56 development of vertical plasma gradients, which result from abrupt enhancements in the  
57 nighttime F-region vertical drift velocity. This process often occurs in conjunction with a  
58 triggering mechanism at the F-region base, typically linked to atmospheric gravity waves and  
59 Large-Scale Wave Structures (LSWS) (Rottger, 1973; Woodman and La Hoz, 1976; Kelley,  
60 2009; Abdu, 1993; Singh et al., 1997a; Taori et al., 2015; Takahashi et al., 2018).

61 During EPB events, the ionosphere can undergo density differences exceeding two orders  
62 of magnitude compared to its initial level. These irregularities diffuse along field lines in both  
63 magnetic hemispheres, reaching the highest latitudes as a result of the maximum vertical  
64 displacement at the magnetic equator (Abdu et al., 1985; Kelley, 2009; Barros et al., 2018). In  
65 this context, EPBs can be studied by analyzing depletions observed in Total Electron Content  
66 (TEC) calculated from Global Navigation Satellite Systems (GNSS) data, as they directly impact  
67 the ionospheric delay experienced by transionospheric electromagnetic waves (Abdu et al., 1985;  
68 Takahashi et al., 2016; Barros et al., 2018). In addition, EPB events can be studied using various  
69 other instruments, including Very High Frequency (VHF) radars (Tsunoda, 1985; Abdu et al.,  
70 2009), ionosondes (Resende et al., 2019), All-Sky imagers (Pimenta et al., 2003; Paulino et al.,  
71 2011; Wrasse et al., 2021), sounding rockets (Abdu et al., 1981; Muralikrishna et al., 2006), and  
72 Earth observation satellites (Huang et al., 2012, 2013; McNamara et al., 2013). Hence, the use of  
73 different instruments enables the study of these irregularities at different longitudes, latitudes,  
74 and altitudes in the ionosphere (Woodman and La Hoz, 1976; Flaherty et al., 1996).

75 The free electrons in the ionosphere can directly influence the propagation of GNSS  
76 signals used in TEC calculation, leading to phase acceleration/delay associated with ionospheric  
77 refraction phenomena (Otsuka et al., 2002; Monico, 2008; Takahashi et al., 2016). The analysis  
78 of this effect is often employed to estimate the amplitude of TEC variation associated with EPB  
79 occurrence, as well as other space weather phenomena (Figueiredo et al., 2018; Wen and Mei,  
80 2020). In this manner, Jakowski et al. (2006) developed the first version of the Disturbance  
81 Ionosphere index (DIX), which relies on the percentage variation of TEC relative to a given

82 quiet reference. This study marked the inception of a new trend of innovative ionospheric  
83 indices, primarily comprising refined versions of the original one, which were achieved through  
84 modifications and the incorporation of new terms into the original equation (Jakowski et al.,  
85 2012a, 2012b, 2019; Wilken et al., 2018; Picanço, 2019; Denardini et al., 2020a; Picanço et al.,  
86 2020; Barbosa-Neto et al., 2022). Consequently, the DIX provides a quantifiable measure of the  
87 ionospheric disturbance level, determined by the variation in TEC associated with ionospheric  
88 phenomena driven by external (e.g., geomagnetic storms) (Denardini et al., 2020a; Picanço et al.,  
89 2021) and internal (e.g., EPBs) (Denardini et al., 2020b; Picanço et al., 2022) sources.

90 This study employs a new methodology to investigate ionospheric variability during EPB  
91 events, based on the DIX methodology as presented in Picanço (2019) and further developed by  
92 Denardini et al. (2020a) and Barbosa-Neto et al. (2020). We initially conducted a comprehensive  
93 identification of EPB-related ionospheric disturbances using GNSS data from approximately 450  
94 stations spanning from the post-peak phase of solar cycle 24 to the pre-peak phase of solar cycle  
95 25 (January 2015 to April 2023). This analysis focused on the geomagnetically quiet days  
96 between September and April of each year, the peak period of EPB occurrence over the South  
97 American region (Barros et al., 2018). Specifically, we focused on the nighttime period, totaling  
98 1321 nights with EPB occurrences, which represents the largest dataset of EPBs ever compiled  
99 for South America using GNSS data. The analysis went beyond merely describing the  
100 morphology of ionospheric disturbances under different solar activity conditions; it also explored  
101 potential physical connections between EPB signatures and the underlying mechanisms  
102 governing their key morphological characteristics, including latitudinal extent, estimated length,  
103 and depletion amplitude. Furthermore, the analysis covered different sectors of magnetic  
104 inclination and declination, seasonal variations, and radiation levels throughout the solar cycle.

105 The results of this study have unveiled several key findings regarding EPBs and their  
106 behavior over the South American region. Firstly, we observed that the amplitude of plasma  
107 depletions and the EPB latitudinal development follow an approximately 11-year cycle driven by  
108 solar radiation levels. During periods of low solar activity, the EPB cycle commences, with  
109 bubble edges closer to the magnetic equator and smaller plasma depletion amplitudes. As solar  
110 activity intensifies, EPB edges move away from the magnetic equator, reaching maximum  
111 latitudes, and the amplitude of plasma depletion increases. Subsequently, as solar activity  
112 diminishes, EPB edges return to near the magnetic equator, reaching a minimum observed  
113 latitude, and plasma depletions decrease in magnitude. Additionally, our analysis highlights the  
114 significant influence of factors such as vertical plasma drift velocity during the pre-reversal  
115 enhancement (PRE), longitudinal variations associated with magnetic declination, as well as the  
116 saturation behavior of EPB development with extreme solar flux. Lastly, we outline an empirical  
117 model to calculate the maximum latitudinal extent of EPBs based on solar flux and magnetic  
118 declination as an attempt to provide insights for anticipating EPB behavior across different solar  
119 cycle stages and in different longitude sectors.

120

## 121 **2 Methodology**

### 122 2.1 DIX calculation

123 In this study we utilized the latest DIX methodology, which combines approaches  
124 presented in Picanço (2019), Denardini et al. (2020a), and Barbosa-Neto et al. (2022). We used

125 the DIX to analyze EPB-related ionospheric disturbances over South America from January 2015  
 126 to April 2023, covering the post-peak phase of solar cycle 24 to the pre-peak phase of solar cycle  
 127 25. It is worth mentioning that days marked by geomagnetic disturbances, wherein the daily sum  
 128 of the Kp index exceeds 24, have not been considered in our analysis. Hence, this study  
 129 investigates EPB events that occur during geomagnetically quiet periods, marking it as the first  
 130 of its kind to employ the DIX index for climatological purposes. Therefore, an in-depth analysis  
 131 of ionospheric disturbances related to EPBs is undertaken, with emphasis on their seasonal,  
 132 latitudinal, longitudinal, and solar activity-induced variations.

133 The DIX is calculated using Equation (1) as follows (Picanço, 2019; Denardini et al.,  
 134 2020a; Barbosa-Neto et al., 2022):

$$DIX_k(t) = \left| \frac{\alpha_k(\Delta TEC_k(t)/TEC_k^{Qd}(t)) + \Delta TEC_k(t)}{\beta} \right|, \quad (1)$$

135 where  $\Delta TEC_k(t) = TEC_k(t) - TEC_k^{Qd}(t)$  is the difference between the measured vertical TEC  
 136 and the non-perturbed reference, both at a given Ionospheric Pierce-Point (IPP),  $k$ . Thus, the  
 137 term  $TEC_k(t)$  represents the vertical TEC calculated for each IPP at a particular time,  $t$ . The  
 138 term  $TEC_k^{Qd}(t)$  represents the non-perturbed reference value for the same IPP and time. The  
 139 value of  $TEC_k^{Qd}(t)$  is determined from the 3-hour TEC moving average obtained during the  
 140 most geomagnetically quiet day within a 15-day window centered on the analyzed day, as  
 141 described by Picanço et al. (2020). The term  $\alpha_k$  represents the  $TEC_k^{Qd}(t)$  for  $t = 0$  (local  
 142 midnight), defined considering the IPP geographic longitude. Finally, the term  $\beta$  corresponds to  
 143 a coefficient dependent on magnetic latitude, which is used to normalize the DIX value on a  
 144 scale ranging from 0 to greater than 5, as determined by the study of maximum ionospheric  
 145 disturbances observed during space weather events of solar cycle 24. The values of coefficient  $\beta$   
 146 are pre-determined and can be obtained from Barbosa-Neto et al. (2022).

148 In Table 1, we present a classification of the ionospheric states according to the DIX  
 149 scale range (Picanço, 2019; Denardini et al., 2020a).

150

151 Table 1 - Classification of ionospheric disturbance states based on the DIX scale.

DIX scale ranges	Ionospheric states
[0 - 1]	Quiet
[1 - 2]	Weakly disturbed
[2 - 4]	Disturbed
[4 - 5]	Exceptionally disturbed
> 5	Extremely disturbed

152

153           Given the above context, it is noteworthy that the DIX methodology provides an  
154 independent value for each individual satellite and time epoch, directly linked to the intensity of  
155 ionospheric disturbance measured at the IPP position. The magnitude of the ionospheric  
156 disturbance recorded in the DIX varies according to the amplitude of changes in TEC relative to  
157 the non-perturbed reference. This magnitude can be higher, as in the case of intense geomagnetic  
158 storm events, or lower, as is the case with EPBs. Thus, it is important to highlight that the DIX is  
159 a sensitive index that simultaneously responds to various space weather phenomena ([Denardini  
160 et al., 2020b](#)). While the DIX sensitivity can be advantageous for space weather monitoring, it is  
161 crucial to select geomagnetically quiet periods during nighttime hours to ensure that we are  
162 studying EPB events with minimal influence from other phenomena.

163

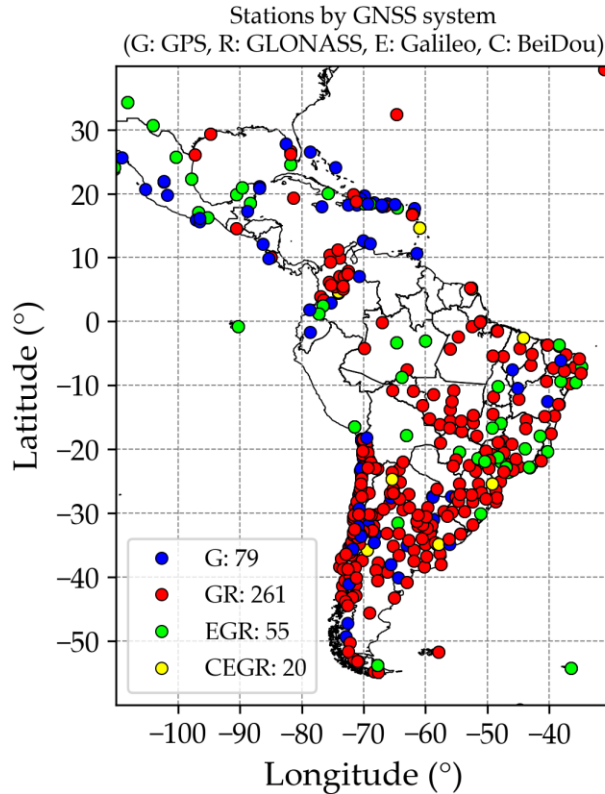
## 164 2.2 Dataset

165           We used data from an average of 450 GNSS stations distributed throughout Latin  
166 America to calculate the DIX for the studied period. These data are freely accessible and  
167 originate from several observation networks including the Brazilian Continuous Monitoring  
168 Network (RBMC, Brazil), University NAVSTAR Consortium (UNAVCO/EarthScope, USA),  
169 National Aeronautics and Space Administration (NASA, USA), Federal Agency for Cartography  
170 and Geodesy (BKG, Germany), Argentine Continuous Satellite Monitoring Network (RAMSAC,  
171 Argentina), Military Geographic Service (SGM, Uruguay), International GNSS Service (IGS,  
172 International), and Low-Latitude Ionospheric Sensor Network (LISN, Peru).

173           The GNSS observables obtained from the available stations were used calculate multi-  
174 constellation and multi-frequency TEC values, following the methodology presented in [Mendoza  
175 et al. \(2019a, 2019b\)](#). Subsequently, the obtained TEC data were used to calculate the DIX index  
176 for each station individually. Therefore, this work utilized DIX index data calculated using the  
177 entirety of available stations, with a sampling rate of 15 seconds. These calculations were based  
178 on four GNSS satellite constellations: GPS, GLONASS, Galileo, and BeiDou, according to the  
179 available data for each period.

180           Figure 1 shows the geographical locations of the GNSS stations used in this study. The  
181 stations are categorized based on the compatibility of the GNSS receivers with the following  
182 constellations: GPS (G: blue circles), GPS and GLONASS (GR: red circles), GPS, GLONASS,  
183 and Galileo (EGR: green circles), and GPS, GLONASS, Galileo, and BeiDou (yellow circles).

184



185

186 **Figure 1:** Geographical locations of the GNSS stations used in the study. Blue circles  
 187 represent stations compatible with GPS, red circles represent stations compatible with GPS and  
 188 GLONASS, green circles represent stations compatible with GPS, GLONASS, and Galileo, and  
 189 yellow circles represent stations compatible with GPS, GLONASS, Galileo, and BeiDou.

190

### 191 2.3 Automatic detection and parameterization of EPB-related ionospheric disturbances

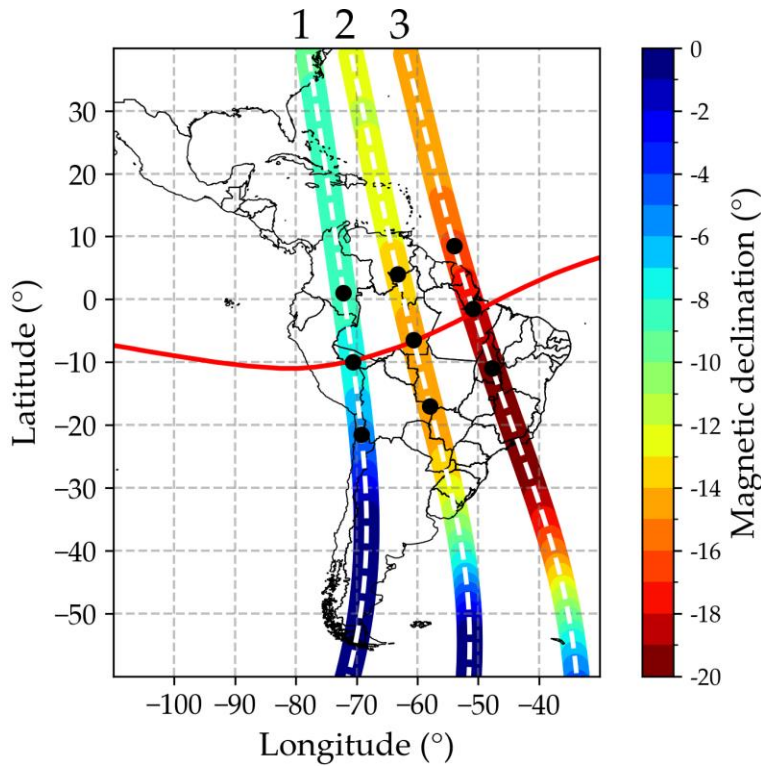
192 After calculating the DIX index for all available stations, we generated interpolated  
 193 observation matrices over a specific region, referred to as DIXMAPs (Denardini et al., 2020a).  
 194 This method facilitates the analysis of spatiotemporal variability in the ionosphere and is  
 195 essential for subsequent stages of the methodology employed in this study, aimed at analyzing  
 196 the morphological characteristics of EPBs. To generate the DIXMAPs, we utilized the technique  
 197 described in Takahashi et al. (2016) to interpolate the DIX data obtained from each available  
 198 GNSS station, assuming a spatial scale of 0.5 degrees. Furthermore, each interpolated matrix  
 199 incorporates 10 minutes of accumulated DIX data to address observation gaps and mitigate data  
 200 failures. The generation of DIXMAPs followed the methodology outlined by Denardini et al.  
 201 (2020a) and Barbosa-Neto et al. (2022).

202 Following the DIXMAP derivation, we proceeded to analyze the latitudinal, longitudinal,  
 203 and temporal variability of ionospheric disturbances associated with EPBs over South America  
 204 by using meridional magnetic cross sections (keograms). These keograms were employed to  
 205 estimate the morphological parameters of the disturbances by using a new automatic  
 206 methodology presented in the following lines. Given that EPBs primarily propagate along

207 geomagnetic field lines, the meridional keograms were constructed based on the coordinates of  
 208 magnetic meridians. To accomplish this, we divided the DIXMAPs domain into three magnetic  
 209 meridians: western, central, and eastern, aiming to examine the variability of EPBs within  
 210 longitudinal sectors and their relationship with magnetic declination angle. This subdivision was  
 211 done through the calculation of magnetic parameters in the DIXMAP domain using the  
 212 International Geomagnetic Reference Field model, version 13 (IGRF-13).

213 Figure 2 illustrates the location of the western (1), central (2), and eastern (3) meridians  
 214 on January 15, 2015. The red line denotes the geographic coordinates of the magnetic equator on  
 215 the same date. The colored dots represent the magnetic declination at points along the meridians.  
 216 It can be observed that the west meridian exhibits low values, the central meridian shows  
 217 intermediate values, and the east meridian shows high values of magnetic declination within the  
 218 DIXMAP domain. Additionally, the black dots represent points with magnetic inclination  
 219 conjugated to the north (+10 degrees magnetic inclination), south (-10 degrees magnetic  
 220 inclination), and magnetic equator (0 degrees magnetic inclination) along each of the meridians,  
 221 which will be used as references in the results section.

222



223

224 **Figure 2:** Geographic coordinates of the western (1), central (2), and eastern (3)  
 225 meridians on January 15, 2015. The red line represents the geographic coordinates of the  
 226 magnetic equator. The colored symbols represent the values of magnetic declination at each of  
 227 the meridian points. The black dots represent points with magnetic inclination conjugated to the  
 228 north ( $10^\circ$ ), south ( $-10^\circ$ ), and magnetic equator ( $0^\circ$ ) along each meridian.

229 With the aim of facilitating the processing of EPB morphological parameters, we  
 230 developed a methodology for the automatic identification and parameterization of ionospheric

231 disturbances related to this phenomenon. The automatic system encompasses the detection of  
 232 EPB-related ionospheric disturbances using the DIX index, followed by the analysis of their  
 233 morphological features. For this purpose, the DIX meridional keograms are utilized individually  
 234 for each night. Any inconsistencies are addressed by cross-referencing the results with data from  
 235 All-Sky imagers and ionosondes, if necessary, following the validation methodology established  
 236 by [Picanço et al. \(2022\)](#).

237 The central approach of this technique involves the binarization of meridional keograms.  
 238 This is achieved by converting the data into binary matrices, where a value of 1 represents the  
 239 presence of EPBs and a value of zero indicates their absence. To do this, it is necessary to define  
 240 a conditional threshold to classify the cells (pixels) of the matrices into binary values. The binary  
 241 threshold (T) is determined using a technique analogous to a high-pass filter, where the cutoff  
 242 value is calculated by identifying the most frequent value within the DIX quiet ionosphere scale.  
 243 The value of T is obtained using Equation (2) below:

244

$$T = M_o(DIX), \text{ if } DIX(x, y) \leq 1, \quad (2)$$

245

246 where  $M_o(DIX)$  represents the statistical mode (the most frequent value) of the DIX  
 247 index within the quiet ionosphere scale (between 0 and 1), obtained for each pixel  $(x, y)$  of the  
 248 keogram.

249 After determining the binary threshold, T, the DIX binary matrix (bin) can be obtained  
 250 using the relationship presented in Equation (3):

251

$$bin(x, y) = \begin{cases} 1, & \text{if } DIX(x, y) > T \\ 0, & \text{if } DIX(x, y) \leq T \end{cases} \quad (3)$$

252

253 Therefore, keogram cells with values greater than the binary threshold will be defined as  
 254 one (disturbances), while cells with values less than or equal to the binary threshold will be  
 255 defined as zero (no disturbances).

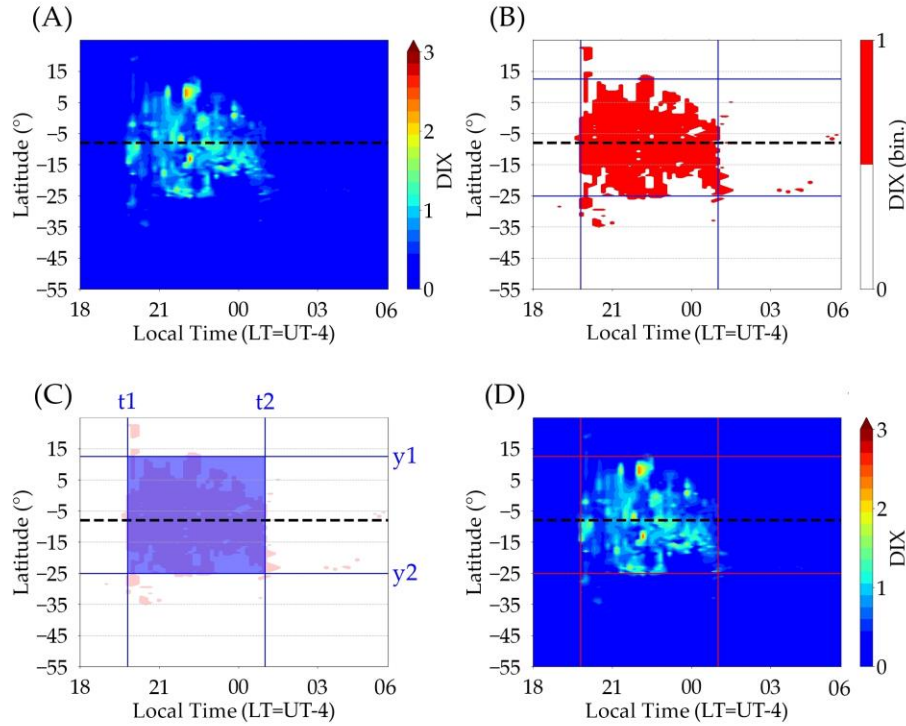
256 After calculating the DIX binary matrix, the methodology proceeds to the disturbance  
 257 edge detection, aiming to estimate features like the time occurrence intervals and their maximum  
 258 latitudinal extent. This is achieved by summing the elements of the binary matrix along both the  
 259 temporal (x-axis) and the latitudinal (y-axis) dimensions.

260 To determine the maximum latitude extent of disturbances, we perform the sum of  
 261 columns of the binary matrix, row by row. If the sum results in a value greater than or equal to  
 262 six time points (where 1 point = 10 min), then the row is classified as 'disturbed'. In this context,  
 263 we declare an EPB occurrence when the disturbance persists for a minimum duration of 1 hour,  
 264 following the criteria adopted by [Barros et al. \(2018\)](#). Thus, disturbed rows with values on the y-  
 265 axis closest to the boundaries of the DIXMAP domain are defined as EPB edges ( $y_1$  and  $y_2$ ),  
 266 while other rows are discarded.

267           The determination of the disturbance time occurrence intervals is performed by summing  
268 the rows of the DIX binary matrix, column by column. If the sum results in a value greater than  
269 or equal to nine latitude points (where 1 point = 0.5 degrees), then the column is classified as  
270 'disturbed.' We declare an EPB occurrence when the disturbance extends more than 500 km  
271 (~4.49 degrees in latitude). Therefore, disturbed columns with values on the x-axis closest to the  
272 temporal boundaries of the nighttime keogram (between 18:00 LT and 06:00 LT) are defined as  
273 disturbance start and end times ( $t_1$  and  $t_2$ ), while other columns are discarded.

274           Both criteria mentioned above are cumulative, and they must be fulfilled to declare the  
275 occurrence of an EPB. Additionally, the edges of the EPBs,  $y_1$  and  $y_2$ , are compared with the  
276 latitude of the magnetic equator on that same magnetic meridian. If there is an asymmetry greater  
277 than 30% in the alignment of the EPBs with the magnetic equator, it is deemed insufficient, and  
278 the data is marked as 'requiring visual analysis,' where we cross-reference the results with data  
279 from All-Sky imagers and ionosondes for further EPB confirmation or rejection.

280           Figure 3 shows an application example of the developed methodology for the automatic  
281 detection and parameterization of EPB-related ionospheric disturbances. Panel 'A' shows the  
282 keogram obtained for the central meridian, showing a region of ionospheric disturbance  
283 characterized by an intensification in the DIX. In Panel 'B', we show the DIX binary matrix  
284 (keogram) obtained through the application of the proposed methodology to the data presented in  
285 the meridional keogram (Panel 'A'), with blue lines marking the disturbance edges. The  
286 disturbance region (Panel 'C') is then defined by delineating the disturbed rows and columns,  
287 where  $y_1$  and  $y_2$  represent the northern and southern edges of the EPB-related disturbances,  
288 while  $t_1$  and  $t_2$  represent the disturbance start and end times, respectively. Finally, Panel 'D'  
289 illustrates the meridional keogram, marked with the edges of the disturbance region. The dashed  
290 black line on the panels represents the geographic latitude of the magnetic equator on the  
291 meridian.



292

293 **Figure 3** - Example of a meridional DIX keogram (Panel 'A') used to generate the binary  
 294 keogram (Panel 'B') and identify the edges of EPB-related ionospheric disturbances (blue lines).  
 295 The coordinates of the disturbed rows and columns used to calculate the occurrence interval ( $t_1$   
 296 and  $t_2$ ) and the latitude extent ( $y_1$  and  $y_2$ ) of the ionospheric disturbances associated with EPBs  
 297 are highlighted (Panel 'C'). Additionally, the meridional keogram marked with the disturbance  
 298 boundaries (red lines, Panel 'D') is shown. The dashed black line represents the geographic  
 299 latitude of the magnetic equator on the meridian.

300

#### 301 2.4 Calculation of EPB latitudinal extent, estimated length, and depletion amplitude

302 After identifying the edges of the EPB-related ionospheric disturbances, it is possible to  
 303 obtain their latitudinal extent (LAT), which represents the range of geographic latitudes between  
 304  $y_1$  and  $y_2$ , as calculated by Equation (4):

305

$$LAT = (y_1, y_2) \quad (4)$$

306

307 The length of the ionospheric disturbances can be estimated using Equation (5):

$$L = d(y_1 - y_2) \quad (5)$$

308 where  $d = 111.19 \text{ km}$  is a conversion factor between degrees ( $^\circ$ ) and kilometers and  
 309 represents the corresponding fraction of the Earth's circumference.

310 At last, the EPB depletion amplitude can be calculated based on the DIX value, as it  
 311 represents the variation of plasma relative to its nonperturbed reference. The depletion amplitude  
 312 (A) is calculated as the DIX value at the average time between  $t_1$  and  $t_2$ , denoted by  $\frac{t_1+t_2}{2}$ , given  
 313 by Equation (6):

$$A = DIX \left( \frac{t_1+t_2}{2} \right) \quad (5)$$

314

### 315 **3 Results and Discussion**

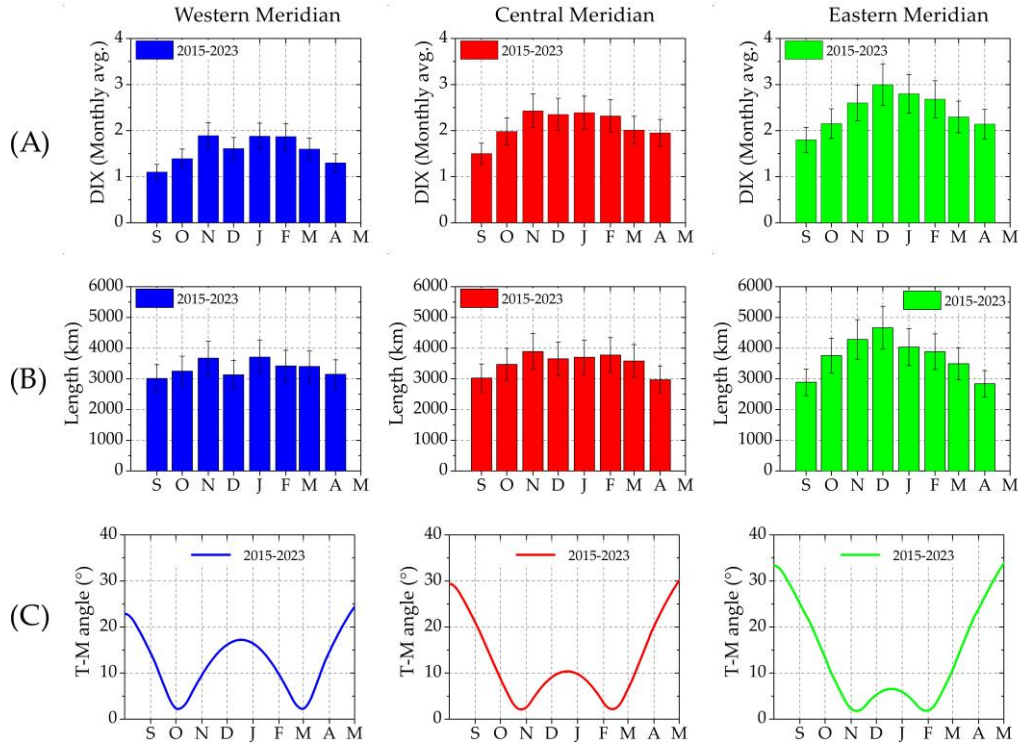
#### 316 **3.1 Seasonal variation of EPB development over different magnetic declination sectors**

317 In this section, we present results from the analysis of the EPB seasonal behavior  
 318 regarding their maximum development during geomagnetically quiet periods over different  
 319 longitude sectors. This analysis utilized data from January 2015 to April 2023 and focused on the  
 320 geomagnetically quiet days between September and April of each year, which is recognized as  
 321 the peak period of EPB occurrence over the South American region. Specifically, we focused on  
 322 the nighttime period, totaling 1321 nights with EPB occurrences, which represents the largest  
 323 dataset of EPBs ever compiled for South America.

324 The length of the EPBs, as well as their latitudinal extent, is intrinsically related to the  
 325 maximum height that the plasma instability reaches at the magnetic equator, since this factor  
 326 controls the distance that the irregular region diffuses along field lines in both magnetic  
 327 hemispheres (Whalen, 2002). In this context, the EPB upward displacement over the equatorial  
 328 region is primarily controlled by the vertical plasma drift velocity during the PRE. According to  
 329 Barros et al. (2018), more intense vertical drift velocities result in a higher RTI growth, leading  
 330 to a greater EPB latitudinal development.

331 In a similar way, some studies suggest that the magnitude of plasma depletion within  
 332 EPBs can be influenced simultaneously by various factors, including the F-region height and the  
 333 amount of background plasma, among others (Singh et al., 1997; Wan et al., 2018). Therefore, a  
 334 better understanding of the seasonal variability and the influence of solar activity on the  
 335 morphological development of EPBs becomes necessary.

336 Figure 4 shows the monthly averages of (A) amplitude depletion and estimated length (B)  
 337 of the EPBs for the western (left panel, in blue), central (middle panel, in red), and eastern (right  
 338 panel, in green) meridians, covering the months between September and April of the dataset.  
 339 Additionally, this figure illustrates the monthly averages of (C) the angle calculated between the  
 340 magnetic meridian and the solar terminator (T-M angle) at 18:00 LT for the three meridians are  
 341 shown. This analysis follows the discussion presented in Abdu et al. (1992), which suggests that  
 342 small angles between the solar terminator and the magnetic meridian result in a higher  
 343 probability of EPBs occurrence.  
 344



345

346 **Figure 4:** Monthly averages of the (A) EPB amplitude depletion between September and April  
 347 from the dataset, together with the averages of the (B) EPB length and the (C) T-M angle, for  
 348 each of the magnetic meridians: western (left column, graphs in blue), central (middle column,  
 349 graphs in red), and eastern (right column, graphs in green).

350

351 The results depicted in Figure 4 confirm a seasonal pattern in the latitudinal and depletion  
 352 aspects of EPB development during geomagnetically quiet periods. This pattern becomes evident  
 353 when comparing the monthly averages of amplitude depletion and EPB length (panels A and B)  
 354 with the T-M angle (panel C). It is observed that the highest lengths and latitudinal extents tend  
 355 to coincide with periods of lower T-M angles. These periods correspond to months with higher  
 356 simultaneity between sunset times in conjugated E regions, leading to increased vertical plasma  
 357 drift velocities, as discussed by Batista et al. (1986). An interesting observation is the more  
 358 pronounced transition curve between these periods (October and March) in the western meridian,  
 359 where the T-M angle reaches 18 degrees near December. This results in a noticeable reduction in  
 360 both the latitudinal development and amplitude depletion of EPBs in this meridian around  
 361 December. Conversely, the amplitude of the T-M angle during the transition period gradually  
 362 decreases across the central and eastern meridians. This behavior results in a more consistent  
 363 development of EPBs during the transition period in these meridians compared to the South  
 364 American western coast, as observed in the length and depletion panels. Additionally, in the  
 365 eastern meridian, the T-M angle approaches 5 degrees during the transition period, which is  
 366 small enough to generate EPBs with the maximum observed development. As emphasized by  
 367 Abdu et al. (1992), the degree of simultaneity between the magnetic meridian and the solar  
 368 terminator plays a crucial role in the occurrence frequency of EPBs. The close alignment of the  
 369 solar terminator with the magnetic meridian results in simultaneous decay of E-region  
 370 conductivity at both ends of the field line, maximizing the strength of the PRE. Our results

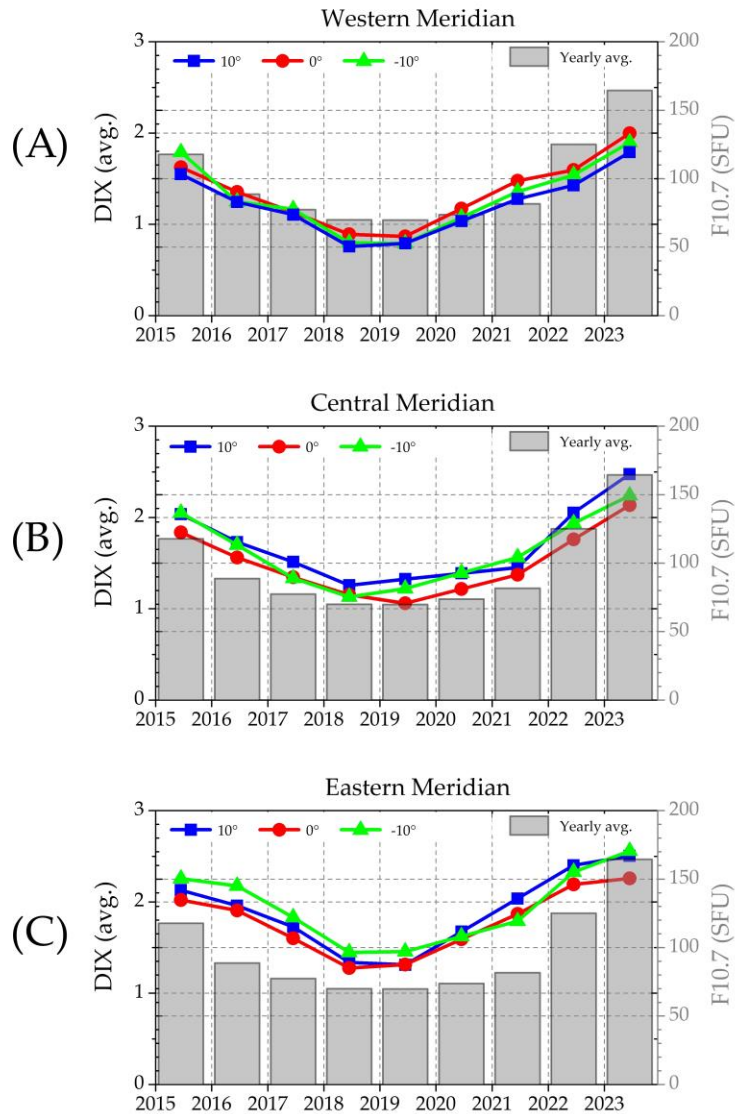
371 further suggest that this aspect also governs the morphological development of these phenomena.  
372 Therefore, it is reasonable to expect that a combination of factors, including the magnitude of  
373 magnetic declination, contributes to the latitudinal development of EPBs. Thus, it is reasonable  
374 to assert that the greater development of EPBs over the eastern South American sector reflects  
375 the higher values of vertical plasma drift throughout the year on this meridian, in contrast to the  
376 western and central meridians (see [Batista et al., 1986](#); [Fejer et al., 2008](#); [Kil et al., 2009](#)).

377

### 378 3.2 Dependence of EPB amplitude depletion on solar flux and magnetic declination

379 Figure 5 depicts the annual averages of the maximum DIX values during EPB events for  
380 each of the magnetic meridians: (A) western, (B) central, and (C) eastern, covering the period  
381 from January 2015 to April 2023. In all panels, the annual averages were calculated for each of  
382 the three conjugate points (as shown in Figure 2), categorized according to their magnetic  
383 inclinations:  $10^\circ$  (symbols in blue),  $0^\circ$  (symbols in red), and  $-10^\circ$  (symbols in green).  
384 Additionally, the panels include gray bars representing the annual averages of the F10.7 index,  
385 expressed in solar flux units (SFU).

386



387  
388

389 **Figure 5:** Annual averages of the maximum DIX values calculated during EPB events at  
390 conjugate points with magnetic inclinations of  $0^\circ$  (red circles),  $10^\circ$  (blue squares), and  $-10^\circ$   
391 (green triangles), obtained in the western (panel 'A'), central (panel 'B'), and eastern (panel 'C')  
392 meridians, from 2015 to 2023. The gray bars represent the annual averages of the F10.7 index  
393 during the same period.

394

395 Based on the results depicted in Figure 5, it is evident that the average curves of  
396 maximum DIX intensity during EPBs exhibit a trend similar to the variation of solar activity  
397 throughout solar cycles 24 and 25. This similarity is highlighted when comparing the average  
398 DIX curves with the annual averages of F10.7 between 2015 and 2019, which span the declining  
399 phase and minimum solar activity of solar cycle 24. During this period, there is a decrease of  
400 approximately 40.78% in the average solar flux intensity, while the DIX demonstrates a decrease  
401 of about 50.46% in the western meridian, 39.21% in the central meridian, and 36.29% in the

402 eastern meridian. Moving into the rising phase of solar cycle 25 between 2019 and 2023, we  
403 observe an increase of approximately 57.60% in the average solar flux intensity. Concurrently,  
404 the DIX shows an increase of about 56.92% in the western meridian, 47.43% in the central  
405 meridian, and 44.18% in the eastern meridian.

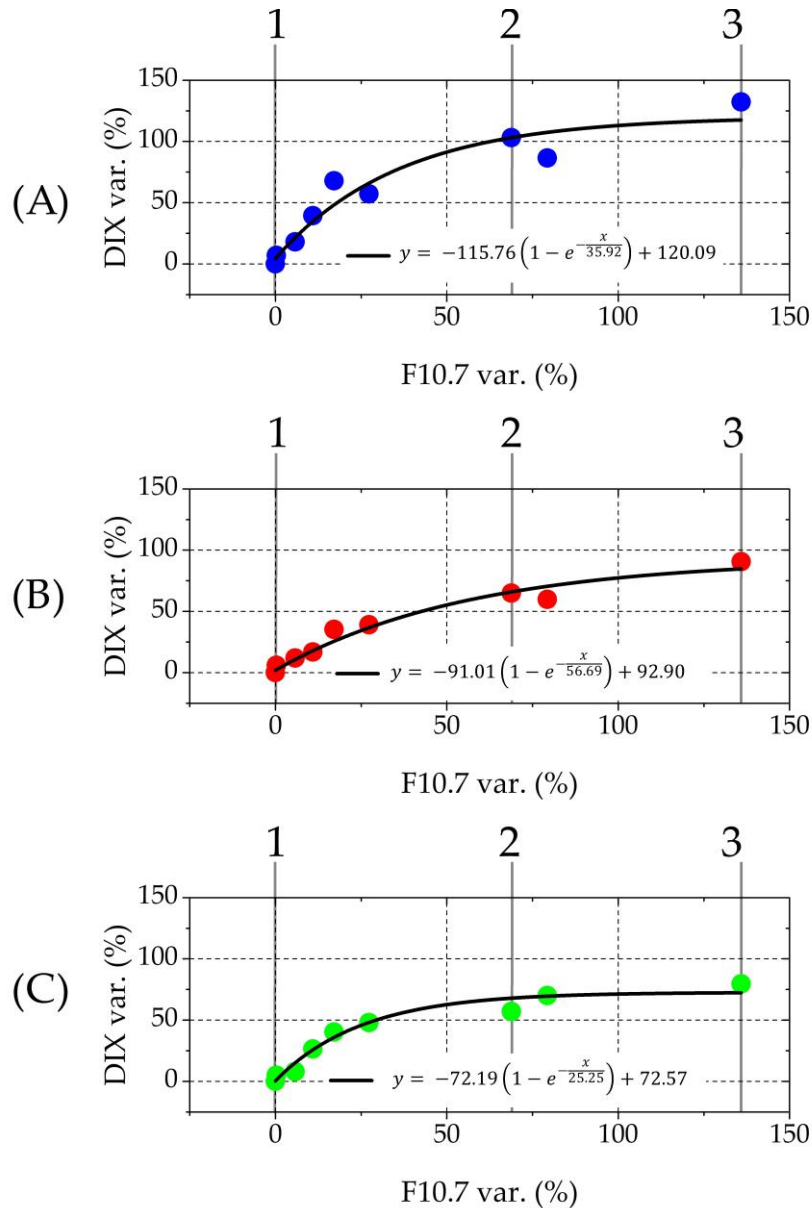
406 The data reveal significant variability in the rate of intensification and weakening of EPB  
407 depletion amplitude in response to changes in solar flux across magnetic meridians in South  
408 America. It is noted that the intensity variation of EPBs in relation to solar flux decreases from  
409 the west coast towards the central meridian, and subsequently to the eastern meridian. As solar  
410 flux increases or decreases, EPBs exhibit distinct trends in each of these regions, highlighting the  
411 substantial influence of geographical location and magnetic declination on the rate of  
412 intensification or weakening of EPBs in response to solar flux variations.

413 Another interesting observation is that when comparing panels A, B, and C from Figure  
414 5, the amplitudes of the annual DIX averages tend to be smaller in the western meridian,  
415 intermediate in the central meridian, and higher in the eastern meridian. This longitudinal  
416 variation correlates with the TEC variation between these sectors, with higher values observed  
417 on the eastern coast compared to the western coast of South America (Nogueira et al., 2013).  
418 Additionally, these differences can be attributed to the strength of the PRE, which is higher on  
419 the eastern coast than on the western coast of South America (Batista et al., 1986). It is  
420 noteworthy that both plasma density and the intensity of the PRE exhibit a strong dependence on  
421 solar flux (Liu et al., 2009; Fejer et al., 2008).

422 The results presented in Figure 5 also indicate that magnetic declination plays a  
423 significant role in the longitudinal variation of EPB depletion, which agrees with the vertical  
424 drift velocity behavior over different declination sectors (Batista et al., 1986). Consequently, the  
425 vertical drift velocity during the PRE period tends to increase with magnetic declination and  
426 exhibits seasonal variations in its intensity peaks (Tsunoda, 1985). Furthermore, Abdu et al.  
427 (1981) noted a similar relationship between EPB occurrence and magnetic declination angle. In  
428 summary, our findings suggest that the amplitude of EPB plasma depletions is proportional to  
429 the intensity of solar energy input into the ionosphere-thermosphere system, which varies as the  
430 solar cycle ascends and descends over an approximately 11-year period (Gnevyshev, 1967).

431 Figure 6 shows the relationship between the percentage rate of change (%) of the DIX  
432 annual averages during EPBs and the F10.7 index for the (A) western, (B) central, and (C)  
433 eastern meridians, covering the period from 2015 to 2023. The rate of change was calculated  
434 based on the data presented in Figure 5, using the values of 2019 (solar minimum) as a fixed  
435 reference. Vertical lines indicate specific stages of the solar flux variation: '1' represents the solar  
436 minimum in 2019, '2' represents the post-peak phase of solar cycle 24 in 2015, and '3' represents  
437 the pre-peak phase of solar cycle 25 in 2023. The solid black lines represent the exponential  
438 function fittings calculated for each magnetic meridian.

439



440

441 **Figure 6:** Scatter plots illustrating the relationship between the percentage rate of change in  
 442 annual averages of the F10.7 index and the DIX during EPBs relative to the solar minimum  
 443 occurring between solar cycles 24 and 25, for the western (A), central (B), and eastern (C)  
 444 meridians. Vertical lines indicate specific stages of the solar cycles: '1' represents the solar  
 445 minimum in 2019, '2' represents the post-peak phase of solar cycle 24 in 2015, and '3' represents  
 446 the pre-peak phase of solar cycle 25 in 2023.

447

448 It is evident that the EPBs depletion amplitude tends to increase with solar activity, as can  
 449 be seen in Figure 6. However, this relationship is not linear and exhibits saturation at high values  
 450 of solar flux. Analysis across the different meridians reveals varying patterns. In the (Figure 6A)  
 451 western meridian, the DIX index increases by approximately 100% ( $DIX \approx 1.65$ ) compared to  
 452 the value observed at solar minimum ( $DIX \approx 0.81$ ), with a corresponding intensification of solar

453 flux by approximately 69.8% (about 117 SFU in 2015). Conversely, in the (Figure 6B) central  
454 meridian, the DIX increase approaches 100% ( $DIX \approx 2.28$ ) relative to the value observed at solar  
455 minimum ( $DIX \approx 1.20$ ), accompanied by a more significant intensification of solar flux,  
456 approximately 135% (about 164 SFU in 2023). Lastly, in the (Figure 6C) eastern meridian, the  
457 DIX increase does not reach 100% compared to the value observed at solar minimum ( $DIX \approx$   
458 1.36), peaking at a maximum variation rate of 79.52% ( $DIX \approx 2.43$ ), with a similar increase of  
459 approximately 135% in solar flux (about 164 SFU in 2023).

460 Upon observing the exponential functions modeled for the western, central, and eastern  
461 meridians of South America, distinct responses emerge concerning the DIX variation in relation  
462 to solar flux. Analysis of the coefficients of the exponential functions reveals notable differences.  
463 The western meridian exhibits a higher rate of EPB intensification, with a coefficient of 115.76,  
464 indicating a more immediate response to changes in solar flux. Saturation is reached with a  
465 120.09% increase in F10.7 intensity compared to the value observed at solar minimum,  
466 representing the peak intensity of EPBs during the period. Beyond this point, the rate of EPB  
467 intensity increase decreases significantly. In contrast, the eastern meridian demonstrates a lower  
468 rate of intensification, with a coefficient of 72.19, indicating a more gradual growth. However,  
469 EPBs reach saturation more readily over the eastern meridian, occurring with a 72.57% increase  
470 in F10.7 intensity compared to the value observed at solar minimum. Additionally, the central  
471 meridian presents an intensification rate of 91.01, with an inflection point at 56.09. In this case,  
472 saturation occurs with a 92.90% increase in F10.7 observed during solar minimum.

473 The analysis of the coefficients of the exponential function for each meridian underscores  
474 a strong relation between the variation in EPB-related depletion amplitudes and longitudinal  
475 sectors. These coefficients offer detailed insights into the distinctive characteristics of each  
476 region concerning the variability of solar flux. The functional analysis reveals diverse response  
477 patterns of EPBs to solar flux variations across South America meridians. The western meridian,  
478 characterized by a rapid initial rate of intensification, demonstrates heightened sensitivity,  
479 ultimately reaching saturation. Conversely, the eastern meridian, despite exhibiting a lower  
480 initial rate, achieves saturation more expeditiously, indicating earlier stabilization compared to  
481 other meridians. Positioned between these extremes, the central meridian shows a notable  
482 equilibrium, manifesting an intermediate initial rate and intensification of solar activity leading  
483 to saturation. These insights gleaned from the exponential functions elucidate the unique features  
484 of each region concerning EPBs, illustrating how distinct meridional sectors respond uniquely to  
485 fluctuations in solar flux.

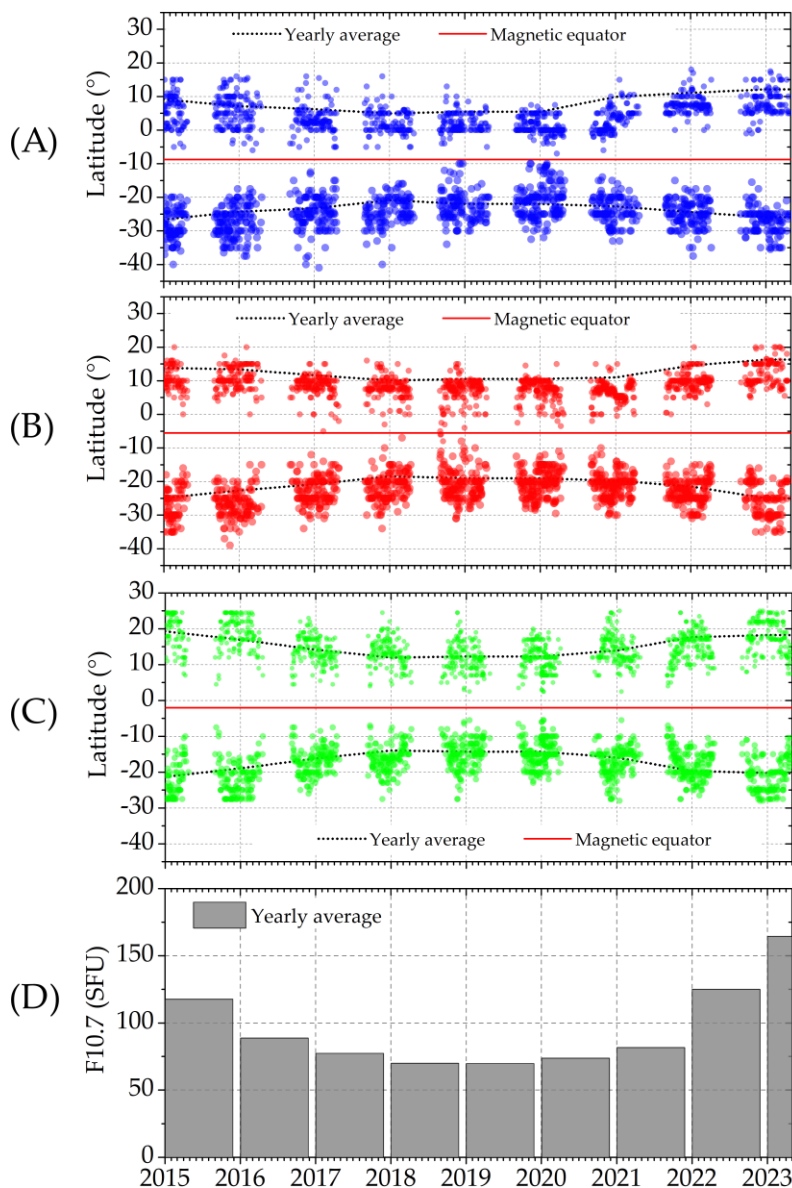
486 From the results presented in Figure 6, it is evident that the saturation point of the  
487 maximum EPB development during geomagnetically quiet periods tends to increase with  
488 magnetic declination. This trend may be attributed to the vertical plasma drift velocity during the  
489 PRE, which governs the amplitude of plasma depletion observed during EPBs. Previous studies  
490 by [Fejer et al. \(1991\)](#) and [Santos et al. \(2013\)](#) have also documented saturation in the  
491 intensification of the PRE peak relative to solar flux across the entire South American sector.  
492 Consequently, sectors with higher declination require lower solar flux levels to achieve the same  
493 maximum vertical drift velocity observed in sectors with lower declination.

494

495 3.3 EPB latitudinal development relation with solar flux and magnetic declination

496 Figure 7 shows the temporal evolution of the maximum latitudinal extent of EPBs from  
 497 2015 to 2023 for the western (A), central (B), and eastern (C) meridians. In each panel, the red  
 498 lines denote the geographic latitude of the magnetic equator for the corresponding meridian.  
 499 Symbols positioned above the magnetic equator line represent the maximum extent of EPBs in  
 500 the northern magnetic hemisphere, while those below represent the maximum extent in the  
 501 southern magnetic hemisphere. Accompanying the symbols are black lines representing the  
 502 annual averages of the maximum latitudinal extensions in each magnetic hemisphere.  
 503 Additionally, gray bars depict the (D) annual averages of the F10.7 index during the same period.

504



505

506

507 **Figure 7:** Temporal variation of the maximum latitudinal extensions reached by EPBs in the  
 508 western (panel A), central (panel B), and eastern (panel C) meridians during the period between  
 509 January 2015, and April 2023. In all panels, the black lines represent the annual averages of the  
 510 maximum extensions, while the red lines represent the latitude of the magnetic equator in each of  
 511 the meridians. The gray bar chart (panel 'D') represents the annual averages of the F10.7 index  
 512 during the same period.

513

514 Figure 7 shows that, like the intensity of the plasma depletions, the EPB latitudinal extent  
 515 also follows the trend of the solar cycle variation. This can be evidenced in panels A, B, and C  
 516 through their comparison with the annual average of the F10.7 index (panel D). In summary, it is  
 517 observed that the edges of the EPBs tend to be displaced from the magnetic equator during  
 518 periods of high solar activity (2015 and 2023) and closer to the magnetic equator during periods  
 519 of low solar activity (2019). These results demonstrate that EPBs develop over a cycle of  
 520 approximately 11 years, which is controlled by the variability of solar activity ([Gnevyshev, 1967](#)).  
 521 In this way, EPBs present lower development in the in the latitudinal and depletion  
 522 aspects during periods of low solar activity, where their edges are closer to the magnetic equator.  
 523 Throughout the ascending phase of the solar cycle, the edges of the EPBs tend to move away  
 524 from the magnetic equator, reaching a maximum possible latitude. Then, in the descending phase  
 525 of the solar cycle, the EPBs begin to approach the magnetic equator again, reaching a minimum  
 526 latitude.

527 Given the direct relationship between the latitudinal extent of EPBs and their maximum  
 528 height at the magnetic equator ([Pimenta et al., 2003](#); [Kelley, 2009](#)), the findings presented in this  
 529 section align with the mechanisms driving the variability in EPB intensity concerning solar  
 530 activity, the intensity of the PRE, and magnetic declination. It is evident that the latitudinal  
 531 extent of EPBs is influenced by solar flux, which fluctuates with the periods of solar activity rise  
 532 and decline. Nevertheless, it is crucial to highlight the existence of a saturation point in EPB  
 533 development concerning solar flux, as discussed in Section 3.2. Thus, we anticipate a saturation  
 534 point in the maximum latitude reached by EPBs.

535

536 3.4 Proposal of an empirical model for EPB latitudinal development under different solar flux  
 537 levels and magnetic declination sectors

538

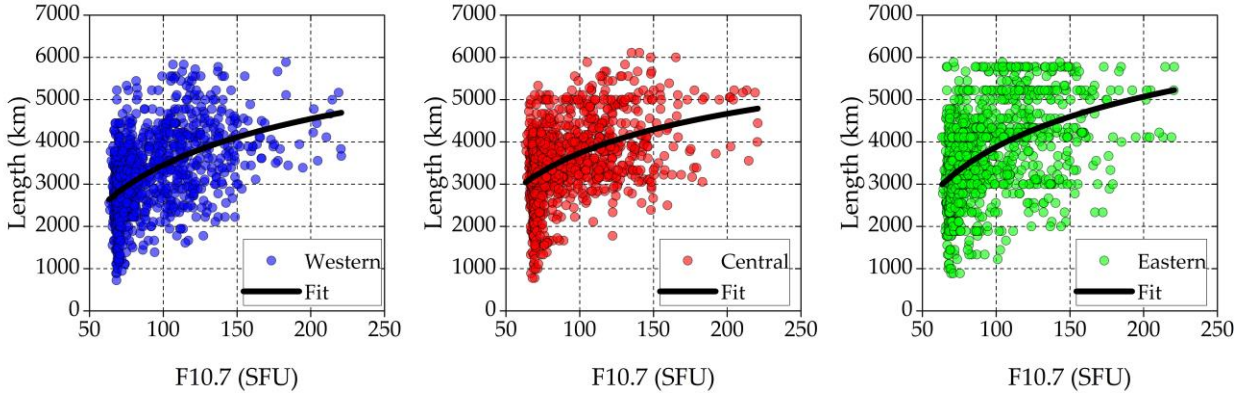
539 In this section, we present the results of a mathematical model concerning the variability  
 540 in the EPB latitudinal development for different levels of solar flux and magnetic declination  
 541 sectors. The model was developed empirically using the data presented in Sections 3.1 to 3.3,  
 542 grounded on theoretical foundations from key studies in the scientific literature on EPB  
 543 development.

544

545 Figure 8 presents the relationship between EPB length (km) and solar flux (SFU), considering  
 546 the data obtained between 2015 and 2023. Each scatter plot includes black lines representing  
 547 logarithmic function fits made to each dataset. Blue plots denote data from the western meridian,  
 548 red plots represent data from the central meridian, and green plots correspond to data from the

549 eastern meridian. The fit equation for these scatter plots is presented and discussed in the  
 550 following lines.

551



552

553 **Figure 8:** Scatter plots representing the relationship between F10.7 values (SFU) and the lengths  
 554 (km) of EPBs from January 2015 to April 2023 for the western meridian (left panel, in blue),  
 555 central meridian (center panel, in red), and eastern meridian (right panel, in green). The black  
 556 lines represent the logarithmic function fits made for each meridian.

557

558 Figure 8 highlights important EPB morphological characteristics. We observe that the  
 559 length increases in response to the intensification of solar flux. However, there is an evident  
 560 saturation tendency in EPB development for high solar flux values. These results agree with  
 561 previous studies, which consider the variability of various equatorial ionospheric  
 562 electrodynamics phenomena as a function of solar activity (Fejer et al., 1991; Nogueira et al.,  
 563 2013; Santos et al., 2013). In this sense, we emphasize that this saturation point is related to the  
 564 physical limits associated with the main EPB generation mechanisms during geomagnetically  
 565 quiet periods, such as PRE, thermospheric wind, and Pedersen conductivity near sunset.

566 Analyzing the results presented in Figure 8, we note that the relationship between the  
 567 latitudinal development of EPBs and solar flux is indeed nonlinear. Another notable  
 568 morphological aspect is the significant variation in EPB length among meridians. Specifically,  
 569 EPBs exhibit greater lengths in the eastern meridian, followed by the central meridian, while  
 570 showing smaller values in the western meridian. This leads to the following observations:

571

- 572     ▪ During the peak of the solar cycle, EPBs reach their maximum development.
- 573     ▪ This development is directly associated with the intensification of irregularity-  
 574         generating mechanisms.
- 575     ▪ The relationship between the intensification of solar flux and EPB development  
 576         follows an increasing, yet nonlinear trend, exhibiting saturation after a certain  
 577         level of solar flux.
- 578     ▪ Longitudinal variation in EPB length is observed, which correlates with the  
 579         magnitude of the magnetic declination angle.

580

581

582

583 The use of logarithmic fits depicted in Figure 8 enabled us to mathematically model the  
 584 latitudinal development of EPBs concerning solar flux and magnetic declination. Thus, we  
 585 employed the fit equation to establish an empirical model for estimating the maximum length  
 586 ( $L_{max}$ ) of EPBs based on solar activity and magnetic declination. Equation 6 presents the  
 587 mathematical expression of the  $L_{max}$  model, denoted in kilometers:

588

$$L_{max} = 1,375a * \ln(-b * \ln(SF)) , \quad (6)$$

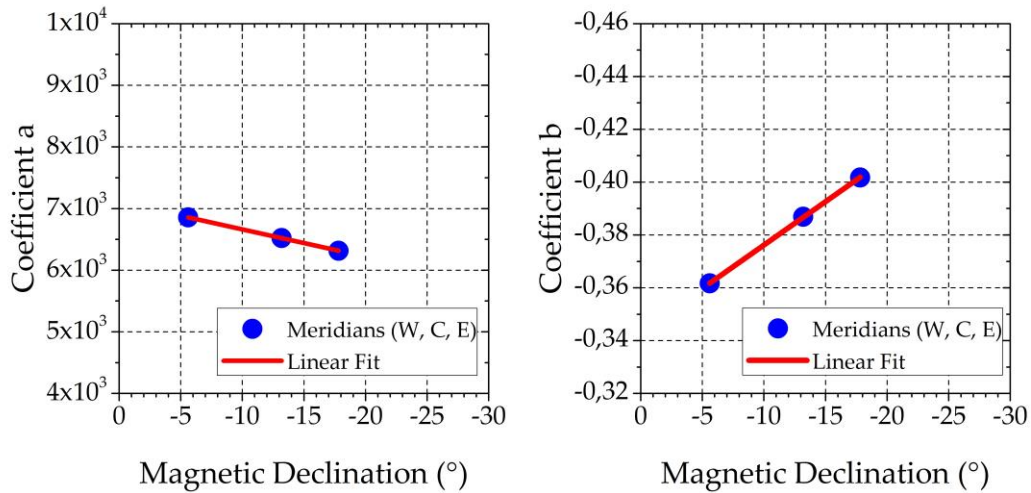
589

590 where  $a$  and  $b$  are the scale and vertical translation coefficients of the logarithmic  
 591 function, individually obtained for each fit presented in Figure 8. SF represents the F10.7 index,  
 592 given in solar flux units (SFU).

593 Below, we demonstrate a method to derive these coefficients as functions of the magnetic  
 594 declination of each meridian, simplifying the calculation process.

595 Figure 9 shows scatter plots of the coefficients  $a$  (left panel) and  $b$  (right panel) obtained  
 596 for each of the three meridians, showing their variation with the magnetic declination of each  
 597 one. The blue symbols, from left to right, represent the meridians from west to east. The red lines  
 598 depict the linear fits obtained for each dataset.

599



600

601 **Figure 9:** Scatter plots depicting the linear relationship between the values of coefficients  $a$  (left  
 602 panel) and  $b$  (right panel) and the magnetic declination of each meridian. The red line in each  
 603 panel represents the linear fit of the obtained function.

604

605

606

607

608 The equations for fitting the coefficients  $a$  and  $b$  are given by:

$$a = 7,1046 \times 10^3 + (44,28(D)) \quad (7)$$

609

$$b = -3,4 \times 10^{-1} + (3,3 \times 10^{-3}(D)) \quad (8)$$

610

611 where  $D$  represents the modulus of the magnetic declination at the magnetic equator latitude.

612

613 The equation for  $L_{max}$  can also estimate the maximum EPB latitudinal extent in both  
614 North and South magnetic hemispheres. This can be done using the following equations:

615

$$y_1 = \frac{1}{2} \left( \frac{L_{max}}{d} \right) + \phi_{eq} \quad (9)$$

616

617

$$y_2 = -\frac{1}{2} \left( \frac{L_{max}}{d} \right) - \phi_{eq} \quad (10)$$

618

619 where  $d = 111.19 \text{ km}$  is the conversion factor between kilometers and degrees ( $^\circ$ ), and  $\phi_{eq}$  is  
620 the latitude of the magnetic equator.

621

622 **4 Summary and Conclusions**

623 In this work we have investigated the morphological characteristics of EPBs and their  
624 relationship with the variability of their generation physical mechanisms. Accordingly, a  
625 methodology based on GNSS data was developed to quantify the variability of ionospheric  
626 plasma during the occurrence of ionospheric disturbances associated with EPBs. This  
627 methodology was applied to study the characteristics of EPBs throughout different stages of  
628 solar cycles 24 and 25, considering various physical aspects of the study area. Therefore, the  
629 results were analyzed with a focus on understanding the nighttime ionospheric electrodynamics  
630 during geomagnetically quiet periods between 2015 and 2023, corresponding to the interval  
631 between the post-peak phase of solar cycle 24 and the pre-peak phase of solar cycle 25. The main  
632 conclusions obtained from this work are summarized as following:

- 633 1. The amplitude of depletion and the latitudinal development of plasma bubbles follow  
634 an approximately 11-year cycle, dictated by solar activity levels. This cycle begins

635 during periods of low solar activity when the edges of these bubbles are closer to the  
636 magnetic equator, and the amplitude of plasma depletions is smaller. As solar activity  
637 increases, the edges of EPBs move farther from the magnetic equator, reaching their  
638 maximum latitudinal extent, while the amplitude of plasma depletions grows.  
639 Subsequently, during periods of decreasing solar activity, the edges of EPBs return  
640 closer to the magnetic equator, reaching a minimum observed latitude, accompanied  
641 by a reduction in the magnitude of plasma depletions.

642 2. The latitudinal extent of EPBs exhibits longitudinal variations associated with  
643 magnetic declination. This factor is related to the degree of simultaneity between the magnetic  
644 meridian and the solar terminator (T-M angle), which controls the time difference between  
645 sunset times at conjugate points in Region E. Therefore, the smaller the T-M angle, the higher  
646 the vertical plasma drift velocity during the occurrence of PRE, resulting in EPBs with greater  
647 latitudinal extent.

648 3. The seasonal variability of EPB intensity shows a dependence on longitudinal sector.  
649 In this context, more intense plasma depletions are observed over the west coast of South  
650 America during the equinox months. On the other hand, on the east coast, the peaks of EPB  
651 intensity exhibit a similar pattern in both equinox and summer months.

652 4. An explanation for the seasonal behavior in EPB intensity is related to differences  
653 between the west and east coasts of South America, both in terms of the amount of plasma in the  
654 environment and the intensity of the PRE. On the west coast, TEC and PRE values reach higher  
655 levels during the equinox months, leading to more intense disturbances in DIX during these  
656 periods. On the other hand, on the east coast, the highest TEC values are observed in the equinox  
657 months, while the peaks of PRE occur during the summer. This configuration results in a less  
658 evident semi-annual variation in EPB intensity along the east coast. As a result, intensity peaks  
659 in DIX occur closer to December in this region, although elevated values are still observed  
660 during the summer months.

661 5. The latitudinal development and amplitude of plasma depletion in EPBs increase as  
662 solar flux intensifies. However, a saturation behavior is observed in this dependence, which is  
663 related to the physical limits associated with the main formation mechanisms of EPBs during  
664 geomagnetically quiet periods, such as PRE, thermospheric wind, and Pedersen conductivity  
665 near sunset.

666 6. An empirical model was developed to calculate the maximum latitudinal extent of  
667 EPBs as a function of solar flux and magnetic declination. This model provides important  
668 information that can be used to estimate EPB development during different stages of the solar  
669 cycle and in different longitudinal sectors.

670

## 671 **Acknowledgments**

672 The authors would like to express their gratitude to the following networks and  
673 organizations for providing the GNSS data essential for this study: RBMC, RAMSAC, LISN,  
674 UNAVCO, NASA, BKG, SGM, and IGS. Special thanks to NASA/OMNIWeb for supplying the  
675 F10.7 data, and to IAGA/NOAA for providing the IGRF-13 model. Additionally, we  
676 acknowledge GFZ Potsdam for the Kp index. G. A. S. Picanço extends sincere thanks to the São  
677 Paulo Research Foundation (FAPESP) for financial support through grant 2023/07518-7, and to

678 Capes/MEC (grants 88887.467444/2019-00 and 88887.685060/2022-00). We are also grateful to  
 679 Barros, D. S., and Wrasse, C. M. for providing the interpolation program utilized in this study.  
 680 Finally, we would like to thank the Brazilian Ministry of Science, Technology, and Innovation  
 681 (MCTI) and the Brazilian Space Agency (AEB) for their support.

## 682 **Data Availability Statement**

683 GNSS data from the networks and organizations mentioned, including RBMC  
 684 (<https://geofitp.ibge.gov.br>), RAMSAC (<https://www.ign.gob.ar>), LISN  
 685 (<http://lisn.igp.gob.pe/jdata>), UNAVCO (<https://data.unavco.org>), NASA  
 686 (<https://cddis.nasa.gov>), BKG (<https://igs.bkg.bund.de>), SGM (<http://www.igm.gub.uy>), and IGS  
 687 (<https://igs.org>), can be accessed through the respective databases of each institution upon prior  
 688 registration. The F10.7 data is available on the NASA/OMNIWeb website  
 689 (<https://omniweb.gsfc.nasa.gov>). The IGRF-13 Python version model can be found on the project  
 690 page (<https://pypi.org/project/pyIGRF>). Additionally, the Kp index can be accessed on the GFZ  
 691 website.

## 692 **References**

- 693
- 694 Abadi, P., Otsuka, Y., & Tsugawa, T. (2015). Effects of pre-reversal enhancement of  $E \times B$  drift  
 695 on the latitudinal extension of plasma bubble in Southeast Asia. *Earth, Planets and Space*,  
 696 67, e74. <https://doi.org/10.1186/s40623-015-0246-7>.
- 697 Abdu, M. A., Bittencourt, J. A., & Batista, I. S. (1981). Magnetic declination control of the  
 698 equatorial F region dynamo field development and spread F. *Journal of Geophysical*  
 699 *Research: Space Physics*, 86(11), 11443–11446.  
 700 <https://doi.org/10.1029/JA086iA13p114403>
- 701 Abdu, M. A., Sobral, J. H. A., Nelson, O. R., & Batista, I. S. (1985). Solar cycle related range  
 702 type spread-F occurrence characteristics over equatorial and low latitude stations in Brazil.  
 703 *Journal of Atmospheric and Terrestrial Physics*, 47(8–10), 901–905.  
 704 [https://doi.org/10.1016/0021-9169\(85\)90065-0](https://doi.org/10.1016/0021-9169(85)90065-0)
- 705 Abdu, M. A., Batista, I. S., & Sobral, J. H. A. (1992). A new aspect of magnetic declination  
 706 control of equatorial spread F and F region dynamo. *Journal of Geophysical Research*,  
 707 97(A10), e14897. <https://doi.org/10.1029/92ja00826>
- 708 Abdu, M. A. (1993). Equatorial spread F and ionosphere–thermosphere system: a review. *Trends*  
 709 *in Geophysics Research*, 2, 193–209.
- 710 Abdu, M. A., Batista, I. S., Reinisch, B. W., Souza, J. R., Sobral, J. H. A., Pedersen, T. R., ...  
 711 Groves, K. M. (2009). Conjugate Point Equatorial Experiment (COPEX) campaign in  
 712 Brazil: electrodynamic highlights on spread F development conditions and day-to-day  
 713 variability. *Journal of Geophysical Research*, 114(A04308).  
 714 <https://doi.org/10.1029/2008JA013749>
- 715 Barbosa-Neto, P. F., Picanço, G. A. S., De Nardin, C. M., Nogueira, P. A. B., Resende, L. C. A.,  
 716 & Moro, J. (2022). Evaluation of the DIX scaling factor during geomagnetically disturbed  
 717 periods over South America. *Brazilian Journal of Geophysics*, 40(4), 1–17.

- 718 <https://doi.org/10.22564/brjg.v40i4.2191>
- 719 Barros, D., Takahashi, H., Wrasse, C. M., & Figueiredo, C. A. O. B. (2018). Characteristics of  
720 equatorial plasma bubbles observed by TEC map based on groundbased GNSS receivers  
721 over South America. *Annales Geophysicae*, 36, 91–100. [https://doi.org/10.5194/angeo-36-](https://doi.org/10.5194/angeo-36-91-2018)  
722 91-2018
- 723 Batista, I. S., Abdu, M. A., & Bittencourt, J. A. (1986). Equatorial F region vertical plasma  
724 drifts: seasonal and longitudinal asymmetries in the American sector. *Journal of*  
725 *Geophysical Research: Space Physics*, 91(A11), 12,055–12,064.  
726 <https://doi.org/10.1029/JA091iA11p12055>
- 727 Denardini, C. M., Picanço, G. A. S., Barbosa-Neto, P. F., Nogueira, P. A. B., Carmo, C. S.,  
728 Resende, L. C. A., ... Bilibio, A. V. (2020a). Ionospheric scale index map based on TEC  
729 data for space weather studies and applications. *Space Weather*, 18, e2019SW002328.  
730 <https://doi.org/10.1029/2019SW002328>
- 731 Denardini, C. M., Picanço, G. A. S., Barbosa-Neto, P. F., Nogueira, P. A. B., Carmo, C. S.,  
732 Resende, L. C. A., ... Bilibio, A. V. (2020b). Ionospheric scale index map based on TEC  
733 data during the Saint Patrick magnetic storm and EPBs. *Space Weather*.  
734 <https://doi.org/10.1029/2019sw002330>
- 735 Fejer, B. G., Gonzalez, S. A., & Woodman, R. F. (1991). Average vertical and zonal F-region  
736 plasma drifts over Jicamarca. *Journal of Geophysical Research: Space Physics*, 96(A8),  
737 13,901–13,906. <https://doi.org/10.1029/91JA01171>
- 738 Fejer, B. G., Jensen, J. W., & Su, S. Y. (2008). Seasonal and longitudinal dependence of  
739 equatorial disturbance vertical plasma drifts. *Geophysical Research Letters*, 35, L20106.  
740 <https://doi.org/10.1029/2008GL035584>
- 741 Flaherty, J. P., Kelley, M. C., Seyler, C. E., & Fitzgerald, T. J. (1996). Simultaneous VHF and  
742 transequatorial HF observations in the presence of bottomside equatorial spread F. *Journal*  
743 *of Geophysical Research: Space Physics*, 101(A12), 26811–26818.  
744 <https://doi.org/10.1029/96JA01115>
- 745 Figueiredo, C. A. O. B., Takahashi, H., Wrasse, C. M., Otsuka, Y., Shiokawa, K., & Barros, D.  
746 (2018). Medium-scale traveling ionospheric disturbances observed by detrended total  
747 electron content maps over Brazil. *Journal of Geophysical Research: Space Physics*, 123,  
748 2215–2227. <https://doi.org/10.1002/2017JA025021>
- 749 Gnevyshev, M. N. (1977). Essential features of the 11-year solar cycle. *Solar Physics*, 51, 175–  
750 183. <https://doi.org/10.1007/BF00240455>
- 751 Haerendel, G., Eccles, J. V., & Cakir, S. (1992). Theory of modeling the equatorial evening  
752 ionosphere and origin of the shear in horizontal plasma flow. *Journal of Geophysical*  
753 *Research*, 97(A2), 1209–1223.
- 754 Huang, C. S., La Beaujardiere, O., Roddy, P. A., Hunton, D. E., Ballenthin, J. O., & Hairston, M.  
755 R. (2012). Generation and characteristics of equatorial plasma bubbles detected by the  
756 C/NOFS satellite near the sunset terminator. *Journal of Geophysical Research*, 117(A11).  
757 <https://doi.org/10.1029/2012ja018163>
- 758 Huang, C. S., La Beaujardière, O., Roddy, P. A., Hunton, D. E., Ballenthin, J. O., Hairston, M.

- 759 R., & Pfaff, R. F. (2013). Large-scale quasiperiodic plasma bubbles: C/NOFS observations  
 760 and causal mechanism. *Journal of Geophysical Research*, 118(6), 3602–3612.  
 761 <https://doi.org/10.1002/jgra.50338>
- 762 Jakowski, N., Stankov, S. M., Schlueter, S., & Klaehn, D. (2006). On developing a new  
 763 ionospheric perturbation index for space weather operations. *Advances in Space Research*,  
 764 38(11), 2596–2600. <https://doi.org/10.1016/j.asr.2005.07.043>
- 765 Jakowski, N., Borries, C., & Wilken, V. (2012a). Introducing a disturbance ionosphere index.  
 766 *Radio Science*, 47(4). <https://doi.org/10.1029/2011rs004939>
- 767 Jakowski, N., Béniguel, Y., De Franceschi, G., Pajares, M. H., Jacobsen, K. S., Stanislawski, I.,  
 768 Tomasik, L., Warnant, R., & Wautelet, G. (2012b). Monitoring, tracking and forecasting  
 769 ionospheric perturbations using GNSS techniques. *Journal of Space Weather and Space*  
 770 *Climate*, 2. <https://doi.org/10.1051/swsc/2012022>
- 771 Jakowski, N., & Hoque, M. M. (2019). Estimation of spatial gradients and temporal variations of  
 772 the total electron content using ground-based GNSS measurements. *Space Weather*, 17,  
 773 339–356. <https://doi.org/10.1029/2018SW002119>
- 774 Kelley, M. C. (2009). *The Earth’s ionosphere: Plasma physics and electrodynamics* (2nd ed.).  
 775 Academic Press.
- 776 Kil, H., Oh, S. J., Paxton, L. J., & Fang, T. W. (2004). High-resolution vertical ExB drift model  
 777 derived from ROCSAT-1 data. *Journal of Geophysical Research*, 114, A10314.  
 778 <https://doi.org/10.1029/2009JA014324>
- 779 Liu, L., Zhao, B., Wan, W., Ning, B., Zhang, M. L., & He, M. (2009). Seasonal variations of the  
 780 ionospheric electron densities retrieved from Constellation Observing System for  
 781 Meteorology, Ionosphere, and Climate mission radio occultation measurements. *Journal of*  
 782 *Geophysical Research*, 114, A02302. <https://doi.org/10.1029/2008JA013819>
- 783 McNamara, L. F., Caton, R. G., Parris, R. T., Pedersen, T. R., Thompson, D. C., Wiens, K. C., &  
 784 Groves, K. M. (2013). Signatures of equatorial plasma bubbles in VHF satellite  
 785 scintillations and equatorial ionograms. *Radio Science*, 48(2), 89–101.  
 786 <https://doi.org/10.1002/rds.20025>
- 787 Mendoza, L. P. O., Meza, A. M., & Aragón Paz, J. M. (2019a). A multi-GNSS, multi-frequency  
 788 and near real-time ionospheric TEC monitoring system for South America. *Space Weather*.  
 789 <https://doi.org/10.1029/2019sw002187>
- 790 Mendoza, L. P. O., Meza, A. M., & Aragón Paz, J. M. (2019b). Technical note on the multi-  
 791 GNSS, multi-frequency and near real-time ionospheric TEC monitoring system for South  
 792 America. *EarthArXiv*. <https://doi.org/10.31223/osf.io/3vts6>
- 793 Muralikrishna, P., & Abdu, M. A. (2006). Rocket measurements of ionospheric electron density  
 794 from Brazil in the last two decades. *Advances in Space Research*, 37(5), 1091–1096.  
 795 <https://doi.org/10.1016/j.asr.2006.02.006>
- 796 Monico, J. F. G. (2008). *GNSS Positioning: Description, Fundamentals, and Applications* (2nd  
 797 ed.). UNESP.
- 798 National Oceanic and Atmospheric Administration (NOAA). (2023). Solar cycle progression.  
 799 Retrieved from <https://www.swpc.noaa.gov/products/solar-cycle-progression>. Accessed

800 August 21, 2023.

- 801 Nogueira, P. A. B., Abdu, M. A., Souza, J. R., Bailey, G. J., Batista, I. S., Shume, E. B., &  
802 Denardini, C. M. (2013). Longitudinal variation in Global Navigation Satellite Systems  
803 TEC and topside ion density over South American sector associated with the four-peaked  
804 wave structures. *Journal of Geophysical Research: Space Physics*, 118(12), 7940–7953.  
805 <https://doi.org/10.1002/2013ja019266>
- 806 Otsuka, Y., Ogawa, T., Saito, A., et al. (2002). A new technique for mapping of total electron  
807 content using GPS network in Japan. *Earth, Planets and Space*, 54, 63–70.
- 808 Paulino, I., Medeiros, A. F., Buriti, R. A., Takahashi, H., Sobral, J. H. A., & Gobbi, D. (2011).  
809 Plasma bubble zonal drift characteristics observed by airglow images over Brazilian tropical  
810 region. *Brazilian Journal of Geophysics*, 29(2), 239–246. [https://doi.org/10.1590/S0102-  
811 261X2011000200003](https://doi.org/10.1590/S0102-261X2011000200003)
- 812 Picanço, G. A. S. (2019). Development and analysis of an ionospheric index based on Total  
813 Electron Content data (Master's thesis, Space Geophysics/Solar-Terrestrial Environmental  
814 Sciences). National Institute for Space Research.
- 815 Picanço, G. A. S., Denardini, C. M., Nogueira, P. A. B., Barbosa-Neto, P. F., Resende, L. C. A.,  
816 Carmo, C. S., Romero-Hernandez, E., Chen, S. S., Moro, J., & Silva, R. P. (2020).  
817 Evaluation of the non-perturbed TEC reference of a new version of the DIX. *Brazilian  
818 Journal of Geophysics*, 38(3), 1–10. <https://doi.org/10.22564/rbgf.v38i3.2056>
- 819 Picanço, G. A. S., Denardini, C. M., Nogueira, P. A. B., Barbosa-Neto, P. F., Resende, L. C. A.,  
820 Chen, S. S., Carmo, C. S., Moro, J., Romero-Hernandez, E., & Silva, R. P. (2021).  
821 Equatorial ionospheric response to storm-time electric fields during two intense  
822 geomagnetic storms over the Brazilian region using a Disturbance Ionosphere index.  
823 *Journal of Atmospheric and Solar–Terrestrial Physics*, 223, e105734.  
824 <https://doi.org/10.1016/j.jastp.2021.105734>
- 825 Picanço, G. A. S., Denardini, C. M., Nogueira, P. A. B., Resende, L. C. A., Carmo, C. S., Chen,  
826 S. S., Barbosa-Neto, P. F., & Romero-Hernandez, E. (2022). Study of the equatorial and  
827 low-latitude total electron content response to plasma bubbles during solar cycle 24–25 over  
828 the Brazilian region using a Disturbance Ionosphere index. *Annales Geophysicae*, 40, 503–  
829 517. <https://doi.org/10.5194/angeo-40-503-2022>
- 830 Pimenta, A., Bittencourt, J., Fagundes, P., Sahai, Y., Buriti, R., Takahashi, H., & Taylor, M. J.  
831 (2003). Ionospheric plasma bubble zonal drifts over the tropical region: A study using OI  
832 630nm emission all-sky images. *Journal of Atmospheric and Solar-Terrestrial Physics*,  
833 65(10), 1117–1126. [https://doi.org/10.1016/S1364-6826Resende, L. C. A.; Denardini, C.  
834 M.; Picanço, G. A. S.; Moro, J.; Barros, D.; Figueiredo, C. A. O. B.; Silva, R. P. On  
835 developing a new ionospheric plasma index for Brazilian equatorial F region irregularities,  
836 \*Annales Geophysicae\*, v. 37, p. 807–818, 2019. <https://doi.org/10.5194/angeo-37-807-2019>.](https://doi.org/10.1016/S1364-6826Resende, L. C. A.; Denardini, C. M.; Picanço, G. A. S.; Moro, J.; Barros, D.; Figueiredo, C. A. O. B.; Silva, R. P. On developing a new ionospheric plasma index for Brazilian equatorial F region irregularities, Annales Geophysicae, v. 37, p. 807–818, 2019. https://doi.org/10.5194/angeo-37-807-2019.)
- 837 Santos, A. M., Abdu, M. A., Sobral, J. H. A., Mascarenhas, M., & Nogueira, P. A. B. (2013).  
838 Equatorial evening prereversal vertical drift dependence on solar EUV flux and F10.7 index  
839 during quiet and disturbed periods over Brazil. *Journal of Geophysical Research: Space  
840 Physics*, 118, 4662–4671. <https://doi.org/10.1002/jgra.50438>

- 841 Singh, S., Bamgboye, D. K., McClure, J. P., & Johnson, F. S. (1997). Morphology of  
842 equatorial plasma bubbles. *Journal of Geophysical Research*, 102(A9), 20019-20029.  
843 <https://doi.org/10.1029/97JA01724>
- 844 Takahashi, H., Wrasse, C., Denardini, C., Pádua, M., PAULA, E., Costa, S., Otsuka, Y.,  
845 Shiokawa, K., Monico, J., Ivo, A., & Sant'anna, N. (2016). Ionospheric TEC weather map over  
846 South America. *Space Weather*, 14, 937-949. <https://doi.org/10.1002/2016SW001474>
- 847 Takahashi, H., Wrasse, C. M., Figueiredo, C. A. O. B., Barros, D., Abdu, M. A., Otsuka,  
848 Y., & Shiokawa, K. (2018). Equatorial plasma bubble seeding by MSTIDs in the ionosphere.  
849 *Progress in Earth and Planetary Science*, 5(32). <https://doi.org/10.1186/s40645-018-0189-2>
- 850 Taori, A., Parihar, N., Ghodpage, R., Dashora, N., Sripathi, S., Kherani, E. A., & Patil, P.  
851 T. (2015). Probing the possible trigger mechanisms of an equatorial plasma bubble event based  
852 on multistation optical data. *Journal of Geophysical Research*, 120(10), 8835–8847.  
853 <https://doi.org/10.1002/2015ja021541>
- 854 Tsunoda, R. T. (1985). Control of the seasonal and longitudinal occurrence of equatorial  
855 scintillations by the longitudinal gradient in the integrated E region Pedersen conductivity.  
856 *Journal of Geophysical Research: Space Physics*, 90, 447-456.  
857 <https://doi.org/10.1029/JA090iA01p00447>
- 858 Wan, X., Xiong, C., Rodriguez-Zuluaga, J., Kervalishvili, G. N., Stolle, C., & Wang, H.  
859 (2018). Climatology of the occurrence rate and amplitudes of local time distinguished equatorial  
860 plasma depletions observed by Swarm satellite. *Journal of Geophysical Research: Space Physics*,  
861 123, 3014–3026. <https://doi.org/10.1002/2017JA025072>.
- 862 Wen, D., & Mei, D. (2020). Ionospheric TEC disturbances over China during the strong  
863 geomagnetic storm in September 2017. *Advances in Space Research*, 65(11), 2529-2539.  
864 <https://doi.org/10.1016/j.asr.2020.03.002>
- 865 Wilken, V., Kriegel, M., Jakowski, N., & Berdermann, J. (2018). An ionospheric index  
866 suitable for estimating the degree of ionospheric perturbations. *Journal of Space Weather and*  
867 *Space Climate*, 8(A19). <https://doi.org/10.1051/swsc/2018008>
- 868 Whalen, J. A. (2002). Dependence of equatorial bubbles and bottomside spread on  
869 season, magnetic activity, and E-region drift velocity during solar maximum. *Journal of*  
870 *Geophysical Research*, 107(A2), 1024. <https://doi.org/10.1029/2001JA000039>
- 871 Woodman, R. F., & La Hoz, C. (1976). Radar observations of F region equatorial  
872 irregularities. *Journal of Geophysical Research*, 81(31), 5447–5466.  
873 <https://doi.org/10.1029/JA081i031p05447>
- 874 Wrasse, C. M., Figueiredo, C. A. O. B., Barros, D., Takahashi, H., Carrasco, A. J., Vital,  
875 L. F. R., Rezende, L. C. A., Egito, F., Rosa, G. M., & Sampaio, A. H. R. (2021). Interaction  
876 between Equatorial Plasma Bubbles and a Medium-Scale Traveling Ionospheric Disturbance,  
877 observed by OI 630 nm airglow imaging at Bom Jesus de Lapa, Brazil. *Earth and Planetary*  
878 *Physics*, 5(5), 397–406. <https://doi.org/10.26464/epp2021045>